First normal stress difference and crystallization in a dense sheared granular fluid

Meheboob Alam[(1)] and Stefan Luding[(1,2)]

[1] *Institut für Computeranwendungen 1, Pfaffenwaldring 27, 70569 Stuttgart, Germeny*

[2] *Particle Technology, DelftChemTech, TU-Delft,*

Julianalaan 136, 2628 BL Delft, The Netherlands

(August 28, 2002)

The first normal stress difference ($\mathcal{N}_1$) and the microstructure in a dense sheared granular fluid are probed using event-driven simulations. $\mathcal{N}_1$ is known to be *positive* (if the stress is defined in *compressive* sense) in a granular fluid and also in elastic hard-sphere fluids. Here we show that $\mathcal{N}_1$ changes sign in the dense limit, and the *origin* of $\mathcal{N}_1$ is tied to the anisotropy in the collision-angle distribution. This sign-reversal of $\mathcal{N}_1$ occurs due to the *microstructural* reorganization of the particles, which can be correlated with a preferred value of the *average* collision angle $\theta_{av} = \pi/4 \pm \pi/2$ in the direction opposing the shear. While the anisotropy in the second moment of fluctuation velocity, which is a Burnett-order effect, is known to be the progenitor of normal stress differences in *dilute* granular fluids, we show here that the collisional anisotropies are responsible for the observed normal stress behaviour in the *dense* limit. We also report on *crystal*-formation, signalling the onset of fluid-solid coexistence in dense granular fluids. Different approaches to take into account the normal stress differences are discussed in the framework of the relaxation-type rheological models.

I. INTRODUCTION

In the last decade, a lot of research activity took place to unveil the properties of granular materials [1,2], primarily because of their industrial importance, but also due to their fascinating properties. This has unraveled many interesting and so far unresolved phenomena (for example, clustering, size-segregation, avalanches, the coexistence of gas, liquid and solid, etc.). Under highly excited conditions, granular materials behave as a fluid, with prominent *non-Newtonian* properties, like the normal stress differences [3]. While the normal stresses are of *infinitesimal* magnitudes in a simple fluid (e.g. air and water), they can be of the order of its isotropic pressure in a dilute granular gas [4]. From the modelling viewpoint, the presence of such large normal-stress differences readily calls for higher-order constitutive models [5,6] even at the *minimal* level.

Studying the non-Newtonian behaviour is itself an important issue, since the normal stresses are known to be the *progenitors* of many interesting and unique flow-features (e.g. rod-climbing or Weissenberg-effect, die-swelling, secondary flows, etc. [7]) in non-Newtonian fluids. Also, normal stresses can support additional instability modes (for example, in polymeric fluids and suspensions [7–10]), which might, in turn, explain some flow-features of granular fluids. For example, particle-clustering [11–13] has recently been explained from the instability-viewpoint using the standard Newtonian model for the stress tensor [14,12,15].

The kinetic theory of Jenkins & Richman [16] first showed that the *anisotropy* in the second moment of the fluctuation velocities, due to the inelasticity of particle collisions, is responsible for such normal stress behaviour. They predicted that the first normal stress difference (defined as $\mathcal{N}_1 = (\Pi_{xx} - \Pi_{yy})/p$, where Π_{xx} and Π_{yy} are the streamwise and the transverse components of the stress deviator, respectively, and p is the isotropic pressure, see section IIB) is maximum in the dilute limit, decreases in magnitude with density, and eventually approaches zero in the dense limit. Goldhirsch & Sela [4] later showed that the normal stress differences appear only at the Burnett-order-description of the Chapman-Enskog expansion of the Boltzmann equation. Their work has clearly established that the

origin of this effect (in the dilute limit) is *universal* in both atomic and granular fluids, with inelasticity playing the role of a *magnifier* and thus making it a sizeable effect in granular fluids. While the *source* of the normal stress differences in the dilute limit has been elucidated both theoretically and by simulation, its *dense* counterpart has not received similar attention so far. This is an important limit since the *onset* of *dilatancy* (volume expansion due to shear, [17]) can be tied to the normal stress behavior [18].

Previous hard-sphere simulations [19,3,11] did look at the normal stress differences, but they did not probe the *dense* limit in a systematic way. These simulations showed that the first normal stress difference vanishes in the dense limit, in line with the theoretical predictions of Jenkins & Richman [16]. On the other hand, the soft-sphere simulations of Walton & Braun [20], with frictional particles, showed that this quantity can change sign in the same limit. Our work with smooth hard-disks unequivocally demonstrates that $\mathcal{N}_1$, indeed, changes its sign at some critical density in the dense regime, due to the sign-change of its collisional component at a critical density, which depends on the value of the coefficient of restitution (e). More importantly, we show that the origin of $\mathcal{N}_1$ in the dense limit is distinctly different from that in dilute granular gas. We further show that, at the *microstructural*-level, certain topological changes in the *anisotropic* structure of the collision-angle distribution with density are responsible for the observed sign-reversal of $\mathcal{N}_1$.

We use the familiar smooth hard-disk model for an event-driven simulation [21] of the uniform shear flow configuration, focussing mainly on the normal stress behaviour and the microstructure formation as function of the density. The details of the simulation technique and the relevant macroscopic quantities are described in section II. The simulation results on the first normal stress difference, the radial distribution function, the collision angle distribution and the crystalline-structure are presented in section III. Possible modelling approaches to incorporate the normal stress differences are discussed in section IV. In section V we summarize our findings, with suggestions for possible future work.

II. SIMULATION METHOD

We consider a collection of smooth inelastic hard-disks in a square box of size $\tilde{L}$ under uniform shear flow — let $\tilde{x}$ and $\tilde{y}$ be the streamwise and transverse directions, respectively, with the origin of the coordinate-frame being positioned at the centre of the box. The snapshot of a typical simulation, with non-dimensional coordinates, is shown in Fig. $1(a)$. Note that the dimensional quantities are denoted by tildes, and the reference length, time and velocity scales for non-dimensionalization will be specified later in this section.

Let the diameter and the mass of the particle be $\tilde{\sigma}$ and $\tilde{m}$, respectively. The pre- and post-collisional particle velocities of particle 1 are denoted by $\tilde{\mathbf{c}}_1$ and $\tilde{\mathbf{c}}_1'$, respectively. Hence, the velocity of particle j relative to 1 is $\tilde{\mathbf{c}}_{21} = \tilde{\mathbf{c}}_2 - \tilde{\mathbf{c}}_1$. Let $\mathbf{k}_{21} = \mathbf{k}$ be the unit vector directed from the center of particle 2 to that of particle 1 at contact. The pre- and post-collisional velocities are related by the expression:

$$\mathbf{k}\cdot\tilde{\mathbf{c}}_{21}' = -e(\mathbf{k}\cdot\tilde{\mathbf{c}}_{21}), \tag{1}$$

where e is the coefficient of normal restitution, with $0 \leq e \leq 1$; note that we restrict ourselves to perfectly smooth particles. The expression for the collisional impulse is

$$\tilde{\mathbf{I}} \;=\; \tilde{m}(\tilde{\mathbf{c}}_1' - \tilde{\mathbf{c}}_1) \;=\; \frac{\tilde{m}}{2}(1+e)(\mathbf{k}\cdot\tilde{\mathbf{c}}_{21})\mathbf{k}, \tag{2}$$

directed along $\mathbf{k}$.

A. Model system and algorithm

The system is periodic in $\tilde{x}$-direction, i.e. a particle crossing the left/right boundary re-enters the system through the opposite boundary at the same vertical position with unchanged velocities. To impose a uniform shear rate ($\tilde{\gamma} = \tilde{U}/\tilde{L}$) in the $\tilde{y}$-direction, the top and bottom image boxes, bounding the central box, are set in motion with velocities $\tilde{U}/2$ and $-\tilde{U}/2$, respectively, in the streamwise direction. This is the standard approach to attain the state of uniform shear flow (USF) by imparting momemtum transfer by shearing, originally

introduced by Lees & Edwards [22]. Overall, this system represents an *extended doubly-periodic* system where the periodicity in the transverse direction is in the local Lagrangian frame. In a typical simulation, the disks are initially placed randomly in the computational box, and the initial velocity field is composed of the uniform shear and a small Gaussian random part. An event-driven algorithm [21] is then used to update the system in time, the details of which may be found in Alam & Luding [23].

To ascertain whether the system has reached the statistical steady-state, the time evolution of the average fluctuation kinetic energy ('granular' energy, defined in the next section) is monitored, see Fig. 1(b). Due to the balance between the shear work and the collisional dissipation under homogeneous shear deformation, the granular energy attains a constant value at the steady state. Depending on the value of the coefficient of restitution and the number of particles, it takes about thousand collisions per particle to reach such a statistical steady-state – the lower the value of e, the more quickly the system reaches the steady state and *vice versa*. The simulation is then allowed to run for another 15000 collisions per particle to gather data to calculate the macroscopic quantities. A few longer runs (30000 collisions per particle) were also checked, with no significant change on the measured quantities. Another quantity which was simultaneously monitored, along with granular energy, is the linearity of the streamwise velocity profile across the Couette gap, and we found that the calculated shear rate (i.e. the slope of the velocity profile) fluctuated around the imposed shear rate by at most 1%.

B. Macroscopic quantities

With $\tilde{L}$, $\tilde{\gamma}^{-1}$, $\tilde{\gamma}\tilde{L}$, and $\tilde{m}$, used as the reference length, time, velocity, and mass, respectively, the relevant dimensionless quantities are:

$$\sigma \;=\; \frac{\tilde{\sigma}}{\tilde{L}}, \quad (\mathbf{c}, \mathbf{u}, \mathbf{C}) = \frac{1}{\tilde{\gamma}\tilde{L}}(\tilde{\mathbf{c}}, \tilde{\mathbf{u}}, \tilde{\mathbf{C}}), \quad \mathbf{P} = \frac{\tilde{\mathbf{P}}}{\tilde{\rho}\tilde{\sigma}^2\tilde{\gamma}^2}, \quad T = \frac{\tilde{T}}{\tilde{\sigma}^2\tilde{\gamma}^2}, \tag{3}$$

where $\mathbf{u}$ is the 'hydrodynamic' velocity, $\mathbf{C} = \mathbf{c} - \mathbf{u}$ the fluctuation (peculiar) velocity of particles, $\tilde{\rho}$ the material density of particles, $\mathbf{P}$ the stress tensor, and T the granular energy.

The macroscopic stress, as measured in discrete particle simulations, is a byproduct of the particle-level mechanisms of momemtum transfer. As in the hard-core model of dense gases, the stress is the sum of its kinetic and collisional components. The former arises from the transport of momentum as the particles move through the system carrying their momentum, while the latter is due to the direct interparticle collisions. The homogeneity of the uniform shear flow allows us to calculate the stress by averaging it over the whole computational box [3,23].

The stress, defined in the *compressive* sense, may be decomposed in the standard way:

$$\mathbf{P} = \mathbf{P}^k + \mathbf{P}^c = p\mathbf{1} + \mathbf{\Pi}, \tag{4}$$

where p is the pressure, $\mathbf{\Pi}$ the pressure deviator and $\mathbf{1}$ the unit tensor. From the off-diagonal components of the pressure deviator, we can calculate the *shear viscosity* which relates the rate of strain to the shear stress:

$$\mu = -\Pi_{xy}/\frac{\mathrm{d}u}{\mathrm{d}y}. \tag{5}$$

For the steady uniform shear flow, thus, the dimensionless shear viscosity can also be interpreted as the shear stress due to our adopted scaling, $\mathrm{d}u/\mathrm{d}y = \gamma = 1$. The diagonal components of the pressure deviator can be non-zero, giving rise to normal stress differences. The first normal stress difference is defined as

$$\mathcal{N}_1 = \frac{(\Pi_{xx} - \Pi_{yy})}{p}. \tag{6}$$

Note that we have scaled this quantity by pressure to ascertain its relative magnitude with respect to pressure. For a standard Newtonian fluid, $\mathcal{N}_1 = 0$ and thus $\mathcal{N}_1$ is an indicator of the *non-Newtonian* character of the fluid. $\mathcal{N}_1$ can be decomposed into kinetic and collisional parts:

$$\mathcal{N}_1 = \mathcal{N}_1^k + \mathcal{N}_1^c = \frac{(\Pi_{xx}^k - \Pi_{yy}^k)}{p} + \frac{(\Pi_{xx}^c - \Pi_{yy}^c)}{p}. \tag{7}$$

Note that the *sign* of $\mathcal{N}_1$ crucially depends on the convention used to define the stress tensor. For example, in the rheology literature, stress is typically defined in the *tensile* sense

[7]. A positive $\mathcal{N}_1$ for the compressive case is equivalent to its negative value for the tensile case and vice versa. This point should be kept in mind while making any comparison with data in the rheology literature.

From the trace of the kinetic stress tensor, $\mathbf{P}^k$, one can calculate the granular energy,

$$T = \frac{1}{2\sigma^2}\left[\frac{1}{N}\sum_{i=1}^{N} C_i C_i\right], \tag{8}$$

which is a measure of the random motion of the particles with respect to the mean motion.

There are two dimensionless control parameters: the volume fraction of particles (ν) and the coefficient of normal restitution (e). The shear rate is also a control parameter, however, due to normalization we have $\gamma = \tilde{\gamma}/\tilde{\gamma} = 1$, and changing the value of $\tilde{\gamma}$ does not influence the reported results; the imposed shear rate γ is thus kept fixed at unity. The simulations are carried out for the whole range of solid volume fractions, varying from the dilute to the dense limit, over a large range of values for the coefficient of restitution ($e = 0.3$–0.99). For most of the simulations, the number of particles are fixed to $N = 1024$, and increasing the value of N by fourfold ($N = 4096$) did not affect the reported quantities noticeably.

For the typical simulation in Fig. $1(a)$, at steady-state, after 2×10^7 collisions, the parameter values were $\nu = 0.5$, $N = 1024$ and $e = 0.7$. The variations of the granular energy T and the calculated shear rate γ_{cal} with time are shown in Fig. $1(b)$, along with corresponding initial variations in two insets. (The data represent the instantaneous values of T and γ_{cal} sampled at a regular interval of 400 collisions – no time averaging is involved here.) It is observed that the granular energy reaches its steady value ($T = 0.6121 \pm 0.022$) quickly after the initial transients and the calculated shear rate fluctuates around its imposed value ($\gamma = 1$) by about $\pm 1\%$. The fluctuations in both T and γ_{cal} at steady-state are due to the finite-size of the system and diminish with increasing number of particles as $N^{-1/2}$.

III. RESULTS

For detailed results on the quantities, pressure, shear viscosity and granular energy, and for their comparison with kinetic theory predictions, we refer to our recent study [23]. Here,

we will mainly focus on the behaviour of the first normal stress difference and its kinetic and collisional components. We also present results on the pair distribution function and the collision angle distribution to characterize microstructures. Lastly we will present some results on *crystal*-formation at high densities, signalling the coexistence of fluid and solid, complementing recent results in non-sheared systems [24,25].

A. Normal stress difference

Figure 2(a) shows the variation of the first normal stress difference ($\mathcal{N}_1$) with density for two values of the coefficient of restitution. It is observed that $\mathcal{N}_1$ is maximum at the dilute limit and decreases thereafter with ν. The overall variation of $\mathcal{N}_1$ with density looks similar at other values of the coefficient of restitution, with a difference in the magnitude of $\mathcal{N}_1$. The inset in Fig. 2(a) shows that $\mathcal{N}_1$ decreases quite sharply in the dense limit and becomes negative at some density ($\nu = \overline{\nu}$). Increasing the value of the restitution coefficient decreases this critical density $\overline{\nu}$. The arrows on the left-ordinate indicate the asymptotic values of $\mathcal{N}_1$ for a two-dimensional granular gas in the dilute limit:

$$\mathcal{N}_1 = \begin{cases} \frac{32(1-e)}{16+9(1-e)} & \text{(Jenkins \& Richman 1988)} \\ \\ 1.0448(1-e^2) & \text{(Sela et al. 1996)} \end{cases} \tag{9}$$

The anisotropy in the second moment of the fluctuation velocity is *primarily* responsible for the finite normal stress difference in the dilute limit [16,26] and this shows up only at the Burnett-order of the Chapman-Enskog expansion [4]. We should mention here that the limit $e \to 1$ is singular and the normal stress difference survives even in the elastic limit as pointed out by Goldhirsch & Sela [4]. The corresponding expression for $\mathcal{N}_1$ in a molecular gas is:

$$\mathcal{N}_1 \approx 1.358 \frac{\gamma^2 \ell^2}{\langle u^2 \rangle},$$

where ℓ is the mean free path and $\langle u^2 \rangle$ is the rms of the velocity fluctuations. However, because of its extremely small magnitude under normal conditions, the normal stress difference is not *measurable* in a molecular fluid.

Previous hard-sphere simulations of Campbell and coworkers [19,3] are in *variance* with our result in that they found $\mathcal{N}_1 \to 0$ as $\nu \to \nu_{max}$. However, the soft-sphere simulations of Walton & Braun [20], with frictional particles, support our observation that $\mathcal{N}_1$ indeed undergoes a *sign-reversal*. To better understand what is responsible for the sign-reversal of $\mathcal{N}_1$, we look at the kinetic and collisional components of the first normal stress difference. Figure 2(b) shows the variations of $\mathcal{N}_1^k$ and $\mathcal{N}_1^c$ with density at $e = 0.7$. We observe that $\mathcal{N}_1^k$ is maximum at the dilute limit and decreases monotonically to zero as ν approaches the packing limit. Except for the dense limit, the overall behaviour of $\mathcal{N}_1^k$ represents that of the total normal stress difference. The collisional component, $\mathcal{N}_1^c$, shows a *non-monotonic* variation with density: $\mathcal{N}_1^c$ is zero in the dilute limit, increases with increasing ν, remains almost constant for intermediate densities, and then decays sharply in the dense limit. Interestingly, $\mathcal{N}_1^c$ becomes negative at some critical density ($\nu = \overline{\nu}$) beyond which the behaviour of $\mathcal{N}_1^c$ mirrors that of $\mathcal{N}_1$ (see inset). Thus the normal stress behaviour in the dense regime is clearly due to the anisotropy in the collisional stresses.

Recall that the kinetic theory of Jenkins & Richman [16,26] predicts that $\mathcal{N}_1 \to 0$ in the dense limit. The predictions of the revised Enskog theory of Santos *et al.* [27] are in line with that of Jenkins & Richman, even though their kinetic model is claimed to be valid even in the crystalline-phase. Since the source of normal stress differences in all these theories is linked to the anisotropy in the second moment of velocity fluctuations (which vanishes as $\nu \to \nu_{max}$), they are unable to predict the correct behaviour of normal stresses in the dense limit.

The sign-reversal of $\mathcal{N}_1^c$ can be succinctly presented as a phase-diagram in the (ν, e)-plane by plotting the zeros of $\mathcal{N}_1^c$ as a function of the coefficient of restitution, see Fig. 3. Below the solid line, $\mathcal{N}_1^c$ is positive, and negative above it. Also plotted in this figure is the line for the zeros of $\mathcal{N}_1$ which, as expected, lies slightly above. The stress tensor is Newtonian

along the solid line which may be called the *symmetry-line*. It is observed that decreasing the coefficient of restitution increases the critical density ($\overline{\nu}$) at which $\mathcal{N}_1^c$ changes sign. As we approach the elastic limit, $\overline{\nu}$ depends strongly on the value of e. We further note that as $e \to 1$, $\overline{\nu} \sim 0.62$ which is well below the freezing-point density of a 2D hard-sphere fluid, $\nu_f \approx 0.70$, [25,24].

We need to mention here that the *sign-change* of $\mathcal{N}_1$ is not uncommon in other non-Newtonian fluids. For example, in non-Brownian viscous suspensions, $\mathcal{N}_1$ changes sign at high Peclet number [28,29]. However, the reason for this effect is quite different in granular fluids as we show below.

B. Microstructural features

Here we probe the microstructural features of a dense granular fluid, with the aim to find out possible relations of the sign-reversal of $\mathcal{N}_1$ with the freezing-transition and the collisional anisotropy. In the last subsection we show some results on the formation of *layered-crystals* with triangular packing.

1. Radial distribution function

Typical snapshots of the system in the dense regime are shown in Fig. 4 at four different densities with $e = 0.7$. Note that for subplot 4(c) the density is $\nu = 0.725$ for which $\mathcal{N}_1^c \approx 0$. Looking at the corresponding distribution of granular energies (not shown here for brevity), we could find signatures of clusters (group of particles) with minimum energies surrounded by particles with maximum energy. To understand the flow-microstructures and their energetics at such high densities, we need to probe the pair distribution function and similar measures for the structure of the packing.

Figure 5(a-d) shows the radial distribution function $g(r)$ at four densities, with parameter values as in Fig. 4. The thin, dotted lines are data from a non-sheared, homogeneous, elastic system [25,24], whereas the thick, solid lines represent a sheared situation with rather strong

dissipation $e = 0.7$. The weak difference at low density $\nu = 0.60$ grows with increasing density, concerning two aspects:

(i) The peak value of contact in the sheared systems is always larger than in a homogenous system of the same density, and the difference increases strongly with density, another indicator for clustering [30].

(ii) The peaks and valleys, which allow to distinguish between different lattice structures, are different in the sheared case when compared to the non-sheared situation. In the former case, peaks at $r/\sigma = 1, 2, 3, \ldots$ are observed, signalling shell-formation about any test-particle. In the latter case, the peaks at $r/\sigma = 1, \sqrt{3}, 2, \ldots$ indicate a crystallization transition and the development of a triangular lattice.

The peaks in the sheared situation, e.g. at $r/\sigma = 2, 3$, become sharper as the density is increased, but the one at $r/\sigma = 4$ is not well-defined even at $\nu = 0.75$; higher order peaks are almost invisible, indicating long-range disorder due to the shearing in contrast to the long-range order that evolves in the non-sheared system. The comparison between the sheared and non-sheared cases suggest that the structure-formation is much slower in a sheared fluid which, in turn, implies that the freezing-point density of the former would be larger than that of the latter. Shear at least delays, if not avoids the freezing of the monodisperse particles to a triangular crystal. The splitting of the second-peak in the non-sheared case corresponds to the *onset* of freezing transition; with increasing density this splitting becomes much more prominent, with similar structural-features appearing at the successively higher-order peaks. The higher-order peaks in the sheared case become prominent only if we go beyond $\nu = \pi/4$, which corresponds to the limit of perfect square-packing, but it is difficult to maintain homogeneous-shearing at such high densities, because the system splits into two parts, a dense, cold, crystalline area and a dilute, hot, fluid area – see below for details.

Furthermore, our simulation data on pressure and viscosity in Fig. 6 show that both increase *monotonically* with density, much beyond $\nu = 0.7001$, and we did not find the *hysteretic* van-der-Walls loop in our pressure data upto $\nu = \pi/4$. These observations, together with our result that in the elastic limit $\mathcal{N}_1$ changes sign at a much lower density ($\nu \approx 0.62$,

see Fig. 3) than the corresponding freezing-density, suggest that the sign-reversal of $\mathcal{N}_1$ is not related to the freezing-transition.

2. Collision angle distribution

Associated with the *sign-reversal* of the first normal stress difference is a change in the relative magnitudes of the normal stress components (P_{xx} and P_{yy}). Subtle changes in the direction and magnitudes of the collisional-mode of momemtum transfer could influence the individual components of the stress tensor. In order to test this hypothesis, we focus on the collision angle distribution function, $C(\theta)$, which is defined such that $C(\theta)d\theta$ is the probability of collision occuring at an angle lying between θ and $\theta + d\theta$ (see, for the definition of θ, Fig. 12). For a fluid in equilibrium, all collisions are equally likely, and hence $C(\theta)$ is a uniform function of θ, *i.e.* $C(\theta) = 1/\pi \approx 0.318309$. For a non-equilibrium system (e.g. shear flow), however, preferred collisions are dictated by the nature of the external field, leading to an anisotropic distribution for $C(\theta)$ [31–33]. Following Savage & Jeffrey [32,33], an explicit expression for $C(\theta; \nu, e)$ can be derived for the case of uniform shear flow as detailed in the Appendix. Note that the angular dependence of $C(\theta; \nu, e)$ will be modified by both the coefficient of restitution and density.

Figure 7 shows the comparison of our simulation data on $C(\theta)$ with the theoretical predictions of equation (A9) for two different values of the coefficients of restitution at a density $\nu = 0.6$. It is observed that the probability of collisions is higher on the *upstream*-faces of the colliding particles, i.e. for $\theta \in [\pi/2, \pi]$ and $\theta \in [-\pi/2, 0]$. This is a consequence of the imposed shear-field which compresses the flow-structure along the $3\pi/4$-direction and stretches along the $\pi/4$-direction. Note that the probability of collisions on the upstream-faces increases further with increasing dissipation levels. Regarding the comparison with theory, there is, clearly, a phase-difference between theory and simulation, and the overall agreement is only qualitative.

Turning our attention to the range of densities where $\mathcal{N}_1$ undergoes a sign-reversal, we

show the collision angle distributions $C(\theta)$ in Fig. 8 as polar plots with $e = 0.7$; the corresponding densities are as in the subplots of Fig. 4. It is observed that the *anisotropic* structure of $C(\theta)$ gets further modified in this regime, with distinct peaks appearing near $\theta = 0$ and $2\pi/3$ (see subplot *b*). While the peak at $\theta = 0$ corresponds to *head-on* collisions between particles in the same-layer, the one at $\theta = 2\pi/3$ clearly signals the *onset* of triangular-structure formation. Another noteworthy point is that the collisions on the downstream-faces of the colliding particles are *rare* at these densities and hence $C(\theta)$ can be approximated solely by its contributions from the second- and fourth-quadrants ($\theta \in [\pi/2, \pi]$ and $\theta \in [-\pi/2, 0]$, respectively).

Since the momemtun transfer occurs mainly due to collisions in the dense regime, the stress tensor can be approximated by

$$\mathbf{P} \sim \int (\mathbf{k} \otimes \mathbf{k}) C(\theta) \mathrm{d}\theta$$

Assuming now that all the collisions would occur at some average collision angle θ_{av} so that $C(\theta) = C(\theta_{av})$, and recalling that $C(\theta)$ is well represented in this regime by restricting θ only in the second- and fourth-quadrants, the expression for the first normal stress differnce simplifies significantly to

$$\mathcal{N}_1 \sim \left[(\mathbf{k} \otimes \mathbf{k})_x - (\mathbf{k} \otimes \mathbf{k})_y\right]_{\theta=\theta_{av}} C(\theta_{av}). \tag{10}$$

It is trivial to check that $\mathcal{N}_1 = 0$ at $\theta_{av} = -\pi/4$. From our simulation data, we have calculated θ_{av} by averaging $C(\theta)$ over the second- and fourth-quadrants, whose variation with density is plotted in Fig. 9 for two restitution coefficients. It is observed that θ_{av} crosses through $-\pi/4$ (i.e. $3\pi/4$) at around the critical density $\overline{\nu}$ for all restitution coefficients. For example, $\theta_{av} \approx -45.16^\circ$ and -45.04° at $\overline{\nu} = 0.725$ and 0.67, respectively, where $\mathcal{N}_1$ changes sign. Thus, the microstructural signature of the sign-reversal of $\mathcal{N}_1$ is directly correlated with the *average* collision angle being greater or less than $-\pi/4$ (or $3\pi/4$).

3. Crystallization: Fluid-solid coexistence

Figure 10(a) shows a snapshot of the system where a solid-layer coexists with a fluidized regime. The parameter values are $\nu = 0.80$ and $e = 0.9$. A closer look reveals that the particles are arranged in a triangular-packing, representing a *crystal*, and thus we have a clear evidence for *fluid-solid* coexistence. The corresponding *instantaneous* streamwise velocity profile is shown in Fig. 10(b); the coarse-graining is done by binning the system into 20 equal-size bins in the transverse direction and then taking averages over all the particles in each bin. Clearly, the shearing is *inhomogeneous* across the Couette-gap: the *layered*-crystal moves with a constant velocity and the shear-rate in the fluidized regimes on either side of the crystal is almost uniform. Note that the velocity profile is *asymmetric*, and this also signals the breakdown of the Lees-Edwards boundary condition as a motor for homogeneous shear. The formation and time-evolution of this crystal can be ascertained from Fig. 10(c) which shows the corresponding evolution of the streamwise velocity at early times. We observe that the crystal has fully formed at $t = 76$, and the velocity profile remains antisymmetric about $y = 0$ till $t = 150$. With further time-evolution, however, the crystal does not remain stationary in the transverse direction, rather it moves slowly with particles diffusing across the fluid-solid interface. The overall life-time of this crystal is several orders of magnitude larger than the external time-scale γ^{-1}, imposed by the shear. The corresponding collision-angle distribution $C(\theta)$, shown in Fig. 10(d), suggests that most of the collisions occurred in the crystalline-phase. (Note that similar layered-microstructure was reported by Campbell & Brennen [33], but due to the small system-size ($N = 40$) and boundary-effects (they considered a shear-flow bounded by walls), the coexistence of fluid and solid is not evident.)

Analogous plots for a nearly elastic system ($e = 0.99$) are shown in Fig. 11(a–c) for the same density $\nu = 0.80$. The overall features are similar to that for $e = 0.9$, but the width of the crystalline zone is a little larger. By decreasing the dissipation-level to $e = 0.7$, we did not observe crystal formation, with other parameters being fixed; by increasing the

system-size to $N = 4096$, however, we observed layered crystal at $e = 0.7$. We should remark here that, at high densities and strong dissipation, the *inelastic collapse* [34,35] terminates the evolution of the system (after some time), however, we do not discuss this artifact of the hard-sphere model. Thus, the formation of such layered-crystalline structure depends crucially on the system size and the dissipation level: *the larger the system-size and the weaker the dissipation, the more susceptiable the system is to crystallize.* Also, even if we are well below the limit of perfect square-packing ($\nu = \pi/6 \approx 0.785$), the system could crystallize if the dissipation-levels are low; for example, we observed signatures of crystalline structures at $\nu = 0.72$ with $e = 0.99$ and $N = 1024$. This indicates that the system relaxes faster/better towards the non-sheared equilibrium situation if dissipation is weaker. However, the steady shear leads to a systematic deviation from that state.

IV. CONSEQUENCES FOR THE CONSTITUTIVE MODELING: RELAXATION MODELS

Here we attempt to describe the normal-stress behaviour of a granular fluid using the standard relaxation-type models. Prior literature on the dense-gas kinetic theory, which forms the foundation of theoretical developments of granular fluids in the *rapid-shear* regime, indicates that such a stress relaxation mechanism does also exist in granular fluids [36–38]. The relaxation-type models are routinely used to describe the non-Newtonian behaviour of viscoelastic/viscoplastic materials, and hence might be apt for granular fluids in the dense limit as well.

Let us consider the viscoelastic relaxation approximation suggested recently by Jin & Slemrod [38] to regularize the Burnett order equations of Sela & Goldhirsch [5] for a low-density granular fluid. Their proposed equation for the pressure deviator, in our notation, is

$$\begin{aligned}\boldsymbol{\Pi} + \tau_1 \left(\frac{D\boldsymbol{\Pi}}{Dt} - \mathbf{L}^T \cdot \boldsymbol{\Pi} - \boldsymbol{\Pi} \cdot \mathbf{L} + \tfrac{2}{d} tr(\boldsymbol{\Pi} \cdot \mathbf{L}) \mathbf{1} \right) \\ + \ \tau_2 \left(\mathbf{S} \cdot \boldsymbol{\Pi} + \boldsymbol{\Pi} \cdot \mathbf{S} - \tfrac{2}{d} tr(\boldsymbol{\Pi} \cdot \mathbf{S}) \mathbf{1} \right) = \boldsymbol{\Pi}^{eq}\end{aligned} \tag{11}$$

where

$$
\begin{aligned}
\mathbf{\Pi}^{eq} &= -2\mu\mathbf{S} - (\lambda\nabla\cdot\mathbf{u})\,\mathbf{1} + \mathbf{\Pi}_2 + \mathbf{\Pi}_3, \\
\mathbf{S} &= \tfrac{1}{2}\left(\mathbf{L} + \mathbf{L}^T\right) - \tfrac{1}{d}\left(\nabla\cdot\mathbf{u}\right)\mathbf{1}, \\
\mathbf{L} &= (\nabla\mathbf{u})^T = \left(\frac{\partial u_i}{\partial x_j}\right) \\
\lambda &= (\zeta - \frac{2}{d}\mu), \\
\tau_1 &= 0.3211\left(\frac{\mu}{p}\right), \\
\tau_2 &= 0.58775\left(\frac{\mu}{p}\right).
\end{aligned}
$$

Here τ_1 and τ_2 are relaxation times, d the dimensionality of the system, $\mathbf{L}$ is the velocity gradient, $\mathbf{S}$ the deviatoric part of the rate of strain tensor, μ the shear viscosity, ζ the bulk viscosity and $\mathbf{1}$ the identity tensor; $\mathbf{\Pi}_2$ and $\mathbf{\Pi}_3$ are higher order terms, explicitly written down in [38]. Note that both relaxation times are proportional to the ratio of the shear viscosity and the pressure, and hence proportional to the mean free path. In the limits of $\tau_1,\ \tau_2 \to 0$ and $\mathbf{\Pi}_2,\ \mathbf{\Pi}_3 \to 0$, we recover the standard Newtonian model for the stress tensor.

Neglecting the higher-order terms, an expression for the first normal stress difference can be obtained for the steady uniform shear flow:

$$
\mathcal{N}_1 = \left[\frac{4\tau_1}{2(1+\tau_1^2) + \tau_2(1+\tau_1-\tau_2)}\right]\left(\frac{\mu}{p}\right) \;>\; 0. \tag{12}
$$

This quantity is always positive, as in our simulation results for dilute flows.

It is important to note that the above evolution equation does not satisfy the *principle of material frame indifference* (MFI) which states that the constitutive laws should be *invariant* under rigid-rotation [7,8]. The scalar field ϕ, the vector field $\mathbf{v}$ and the tensor field $\mathbf{\Pi}$ are called *frame-indifferent* or *objective* if the following relations hold for all t:

$$
\phi'(\mathbf{x}', t') = \phi(\mathbf{x}, t), \tag{13}
$$

$$
\mathbf{v}'(\mathbf{x}', t') = \mathbf{Q}(t)\mathbf{v}(\mathbf{x}, t), \tag{14}
$$

$$
\mathbf{\Pi}'(\mathbf{x}', t') = \mathbf{Q}(t)\mathbf{\Pi}(\mathbf{x}, t)\mathbf{Q}(t)^T, \tag{15}
$$

where ϕ, $\mathbf{v}$ & $\mathbf{\Pi}$ and ϕ', $\mathbf{v}'$ & $\mathbf{\Pi}'$ are defined in two different frames $\mathcal{F}$ and $\mathcal{F}'$, respectively, and $\mathbf{Q}(t)$ is a proper orthogonal tensor. Here $\mathcal{F}' \in \mathcal{E}(\mathcal{F})$, with $\mathcal{E}(\mathcal{F})$ denoting the set of all frames obtainable from a given frame $\mathcal{F}$ by observer transformations. That the stress-tensor in a granular gas is not a frame-independent quantity (as in the hard-sphere gas [39,40]) is well-known. In the framework of the standard relaxation models, this effect shows up as a *sign-change* of the first normal stress difference [23].

If one has to recover the Boltzmann-limit of relaxation-type equations, which is non-objective, a frame-indifferent approach is ruled out. Since the kinetic component of the first normal stress difference remains positive at all densities, the kinetic stress tensor can be modelled using a non-objective equation as discussed above. If we were to postulate a relaxation-type model for the collisional stress tensor as well, then, it must change its type, from *nonobjective* to *objective*, at a critical density as one approaches the dense limit. (For steady homogeneous shear flow, one can also model positive/negative normal stress differences by postulating a general orthonormal basis, generated by the nilpotent basis tensors, which satisfies the objectivity requirement; for related issues, the reader is referred to Goddard [8].)

A question now arises as to the possibility of writing down a single evolution equation for the total stress deviator, $\mathbf{\Pi}$, by combining evolution equations of its kinetic and collisional components. The simplest way to postulate such an equation is:

$$\mathbf{\Pi} + \alpha(\nu, e)\tau \left(\frac{\mathrm{D}\mathbf{\Pi}}{\mathrm{D}t} - \left\{ \mathbf{L}^T \cdot \mathbf{\Pi} + \mathbf{\Pi} \cdot \mathbf{L} - \tfrac{2}{d}\mathrm{tr}(\mathbf{\Pi} \cdot \mathbf{L})\mathbf{1} \right\} \right) = -2\mu\mathbf{S} - (\lambda \nabla \cdot \mathbf{u})\,\mathbf{1}. \tag{16}$$

where $\alpha(\nu, e)$ is an empirical constant, dependent on both density and restitution coefficient. This is nothing but the Jin-Slemrod equation with $\tau_2 = 0$ and neglecting its higher-order terms. Note that the above equation resembles the well-known *lower-convected* equation with a *minus* sign in front of the curly bracket. For this case, the first normal stress difference is

$$\mathcal{N}_1 = \frac{2\tau\alpha}{1 + \tau^2\alpha^2} \left(\frac{\mu}{p} \right). \tag{17}$$

Clearly, if $\alpha(\nu, e)$ is obtained from simulation, its sign-reversal would also correspond to the sign-reversal of $\mathcal{N}_1$.

Another possibility to model $\mathcal{N}_1$ is to postulate the following equation for the pressure deviator:

$$\mathbf{\Pi} + \alpha(\nu, e)\tau \left(\frac{\mathrm{D}\mathbf{\Pi}}{\mathrm{D}t} + \left\{ \mathbf{L}\cdot\mathbf{\Pi} + \mathbf{\Pi}\cdot\mathbf{L}^T - \tfrac{2}{d}\mathrm{tr}(\mathbf{\Pi}\cdot\mathbf{L})\mathbf{1} \right\} \right) = -2\mu\mathbf{S} - (\lambda\nabla\cdot\mathbf{u})\,\mathbf{1}. \qquad (18)$$

With a *minus* sign in front of the curly-bracket and $\alpha(\nu, e) = 1$, this represents the *upper-convected* equation [7]. It can be verified that $\mathcal{N}_1$ is also given by (17) for this case. Similarly, one could postulate evolution equations using other objective derivatives (e.g. Jaumann rate, etc, [7]). Despite its empirical nature and crudeness, such a simplified approach holds promise for practical purposes.

V. SUMMARY AND CONCLUSION

We have probed the non-Newtonian behaviour and the incipient crystalline-phase in a sheared, monodisperse, two-dimensional granular fluid. The standard event-driven technique is used to simulate a box of hard-disks under homogeneous shear deformation. The information about the stress tensor is obtained by decomposing it in the standard way: $\mathbf{P} = p\mathbf{1} + \mathbf{\Pi}$, where p is the pressure and $\mathbf{\Pi}$ the pressure deviator. The non-Newtonian behaviour is quantified in terms of the first normal stress difference: $\mathcal{N}_1 = (\Pi_{xx} - \Pi_{yy})/p$.

The granular fluid is non-Newtonian with measurable first normal stress difference ($\mathcal{N}_1$) which is *positive* (if the stress is defined in the *compressive* sense) in the dilute limit. Interestingly, however, $\mathcal{N}_1$ *changes* from positive to negative at a critical density in the dense regime. By decomposing $\mathcal{N}_1$ into the kinetic and collisional contributions, $\mathcal{N}_1 = \mathcal{N}_1^k + \mathcal{N}_1^c$, we found that while $\mathcal{N}_1^k$ is always positive and decays to zero in the dense limit, $\mathcal{N}_1^c$ has a *non-monotonic* variation with density. In particular, $\mathcal{N}_1^c$ increases from zero in the dilute limit as ν increases, reaches a maximum at some value of ν and then decreases, eventually becoming *negative* in the dense limit. The density at which $\mathcal{N}_1^c = 0$ ($\nu \equiv \overline{\nu}$) depends crucially on the level of micro-scale dissipation; in particular, $\overline{\nu}$ increases as the coefficient of restitution decreases. We have constructed a phase-diagram in the (ν, e)-plane by identifying the regions where $\mathcal{N}_1$ is positive/negative.

At the micro-level, the particles undergo reorganization as the dense-limit is approached. The signatures of microstructural-reorganization have been captured by probing the collision-angle distribution, $C(\theta)$, which is *anisotropic* due to the presence of the mean shear. In particular, we have found that the topology of the anisotropic-structure of $C(\theta)$ changes, with collisions occurring at certain preferred angles on the upstream-faces of the colliding pairs. The *sign-reversal* of $\mathcal{N}_1$ is correlated with a preferred value of the average collision angle, $\theta_{av} = \pi/4 \pm \pi/2$, averaged over the *upstream*-faces of the colliding particles.

We have shown that the *origin* of the first normal stress difference, in the dense limit, is tied to the collisional anisotropies. The underlying mechanism is distinctly different from that is known for a dilute granular gas [16,4] where the anisotropy in the second moment of fluctuation velcoity, which is a Burnett-order effect, gives rise to normal stress differences.

The time evolution of the sheared granular fluid leads to *crystallization* in the dense limit, signalling the *coexistence* of fluid and solid. The particles are arranged in a triangular-packing inside the crystal, and it moves as a *layer* in the streamwise direction. The formation of such layered-crystalline structure depends crucially on the system size and the dissipation level: the larger the system-size and the weaker the dissipation, the more susceptible the system is to crystallize.

The present work clearly shows that the available kinetic-theory-based rheological models for granular fluids are not adequate to predict the behaviour of the first normal stress difference in the dense limit. Certain microstructural-features, like the preferred distribution of collisions which eventually leads to crystal-formation, should be incorporated into the theory. To incorporate the observed normal stress behaviour into the framework of 'plausible' constitutive models, we postulated a relaxation-type evolution equation for the stress deviator. Using frame-dependent derivatives, with empirical fit parameters, the model would be valid over the whole range of densities.

VI. ACKNOWLEDGEMENT

M.A. acknowledges the financial support by the Alexander von Humboldt Foundation and S.L. acknowledges the support of the Deutsche Forschungsgemeinschaft. M.A. is grateful to Hans J. Herrmann for discussions and hospitality at ICA1, and also acknowledges discussions with Joe D. Goddard on certain aspects of normal stress behaviour in granular fluids. We thank John F. Brady for directing us to relevant references on normal stresses in suspensions.

APPENDIX A: SHEAR-INDUCED ANISOTROPY AND THE COLLISION ANGLE DISTRIBUTION

Here we are interested in the shear-induced anisotropy of the collision angle distribution of an inelastic hard-disk fluid. Following Savage & Jeffrey [32] an expression for the collision angle distribution $C(\theta)$ is derived, which is compared with our simulation data in IIB.2.

To calculate the probablility of collisions at a specific angle θ, we focus on Fig. 12 with two particles colliding at $\mathbf{r}$. Note that θ is measured anticlockwise from the positive x-axis. For collisions to occur in a time δt, the center of particle 1 must lie inside the volume $\sigma\delta\mathbf{k}(\mathbf{q}\cdot\mathbf{k})\delta t$, where $\mathbf{q} = \mathbf{c}_1 - \mathbf{c}_2$ is the relative velocity of the colliding pair. Thus the expected total number of collisions (per unit time and unit area) with the line of centres $\mathbf{k}$ lying between $\mathbf{k} - \delta\mathbf{k}/2$ and $\mathbf{k} + \delta\mathbf{k}/2$ is given by

$$\int \sigma f^{(2)}(\mathbf{c}_1, \mathbf{r}_1, \mathbf{c}_2, \mathbf{r}_2)(\mathbf{q}\cdot\mathbf{k})(\mathbf{k}\cdot\mathbf{n}) d\mathbf{k} d\mathbf{c}_1 d\mathbf{c}_2 \tag{A1}$$

where $f^{(2)}(\cdot)$ is the two-particle distribution function which is defined so that $f^{(2)}(\mathbf{c}_1, \mathbf{r}_1, \mathbf{c}_2, \mathbf{r}_2)\ d\mathbf{c}_1 d\mathbf{c}_2 d\mathbf{r}_1 d\mathbf{r}_2$ is the number of pairs of particles such that the particle i is located in an area element $d\mathbf{r}_1$ about $\mathbf{r}_1$ with its velocity in the interval $d\mathbf{c}_1$ about $\mathbf{c}_1$ while particle j is located in an area element $d\mathbf{r}_2$ about $\mathbf{r}_2$ with its velocity in the interval $d\mathbf{c}_2$ about $\mathbf{c}_2$. To progress further, we have to invoke the assumption of molecular chaos and hence the expected number of collisions is

$$\int \sigma g(\mathbf{r}_1, \mathbf{r}_2) f^{(1)}(\mathbf{c}_1, \mathbf{r}_1; \mathbf{u}(\mathbf{r}_1)) f^{(1)}(\mathbf{c}_2, \mathbf{r}_2; \mathbf{u}(\mathbf{r}_2))(\mathbf{q} \cdot \mathbf{k})(\mathbf{k} \cdot \mathbf{n}) d\mathbf{k} d\mathbf{c}_1 d\mathbf{c}_2 \tag{A2}$$

where $g(\mathbf{r}_1, \mathbf{r}_2)$ is the pair-distribution function. For the steady uniform shear flow, $g(\mathbf{r}_1, \mathbf{r}_2)$ is calculated from the relation [31,32,41]:

$$g(\mathbf{r}_1, \mathbf{r}_2) = \frac{2g_c(\nu)}{n^2} \int_{\mathbf{q}\cdot\mathbf{k}>0} f^{(1)}(\mathbf{c}_1, \mathbf{r}_1; \mathbf{u}(\mathbf{r}_1)) f^{(1)}(\mathbf{c}_2, \mathbf{r}_2; \mathbf{u}(\mathbf{r}_2)) d\mathbf{c}_1 d\mathbf{c}_2 \tag{A3}$$

where $g_c(\nu)$ is the *contact* value of the pair-distribution function and $\mathbf{q} \cdot \mathbf{k} > 0$ implies that the integration be carried out for impending collisions.

As a first approximation, the single particle velocity distribution function $f^{(1)}(\mathbf{c}_1, \mathbf{r}_1; \mathbf{u}(\mathbf{r}_1))$ is assumed to have the Maxwellian-form:

$$f^{(1)}(\mathbf{c}_1, \mathbf{r}_1; \mathbf{u}(\mathbf{r}_1)) = \left(\frac{nm}{\pi k_B T}\right) \exp\left[-\frac{m\left(\mathbf{c}_1 - \mathbf{u}(\mathbf{r}_1)\right)^2}{2k_B T}\right] \tag{A4}$$

where T is the granular temperature (fluctuating kinetic energy) and k_B the usual Boltzmann constant. Now transforming the particle velocities ($\mathbf{c}_1$, $\mathbf{c}_2$) to their center-of-mass and relative velocities, equation (A3) can be integrated to arrive at the following explicit expression for the pair-distribution function [32]:

$$g(\mathbf{r}_1, \mathbf{r}_2) = g_c(\nu) \mathrm{erfc}\left[\frac{2\mathbf{k} \cdot \mathbf{u}(\mathbf{r}_2)}{(2k_B T)^{1/2}}\right], \tag{A5}$$

where $\mathrm{erfc}(\cdot)$ is the complementary error function. Using the above expression for the pair-distribution function and transforming in terms of polar coordinates (r, θ), the integral for the normalized collision angle distribution yields [33]

$$C(\theta) = \mathcal{A}(T)\left[\exp\left(-\frac{\sin^2\theta\cos^2\theta}{2T}\right) - \frac{g(\theta)\sin\theta\cos\theta}{\sqrt{T}}\right] g(\theta) \tag{A6}$$

where $g(\theta)$ is the angular pair-distribution function given by

$$g(\theta) \equiv \frac{g(\mathbf{r}_1, \mathbf{r}_2)}{g_c(\nu)} = \mathrm{erfc}\left[\frac{\sin\theta\cos\theta}{\sqrt{2T}}\right] \tag{A7}$$

and $\mathcal{A}(T)$ is a normalization constant.

For the uniform shear flow, an expression for the granular temperature, can be obtained from the energy balance equation, by equating the energy production due to shear-work with the energy loss due to collisions:

$$\mu \frac{du}{dy} = \mathcal{D}$$
$$\Rightarrow T = f_\mu(\nu)/f_\mathcal{D}(\nu, e) \tag{A8}$$

where $\mu = \rho_p \sigma f_\mu(\nu)\sqrt{T}$ is the shear viscosity and $\mathcal{D} = (\rho_p/\sigma) f_\mathcal{D}(\nu, e) T^{3/2}$ the collisional dissipation rate, with

$$f_\mu(\nu) = \frac{\sqrt{\pi}\nu}{8}\left[\frac{1}{\nu g_c(\nu)} + 2 + \nu g_c(\nu)\left(1 + \frac{8}{\pi}\right)\right]$$
$$f_\mathcal{D}(\nu, e) = \frac{4}{\sqrt{\pi}}(1 - e^2)\nu^2 g_c(\nu).$$

Substituting this expression for T, the normalized collision distribution function becomes

$$C(\theta; \nu, e) = \mathcal{A}(T)\left[\exp\left(-\frac{f_\mathcal{D}(\nu, e)\sin^2\theta\cos^2\theta}{2f_\mu(\nu)}\right) - g(\theta)\sin\theta\cos\theta\sqrt{\frac{f_\mathcal{D}(\nu, e)}{f_\mu(\nu)}}\right] g(\theta) \tag{A9}$$

and the angular pair-distribution function

$$g(\theta; \nu, e) = \operatorname{erfc}\left[\sin\theta\cos\theta\sqrt{\frac{f_\mathcal{D}(\nu, e)}{2f_\mu(\nu)}}\right], \tag{A10}$$

It is clear that the angular dependence of $C(\theta; \nu, e)$ is modified by both the inelastic dissipation and the density.

---

[1] H. J. Herrmann, J.-P. Hovi, and S. Luding, editors. *Physics of dry granular media - NATO ASI Series E 350*, Dordrecht, 1998. Kluwer Academic Publishers.

[2] T. Pöschel and S. Luding, editors. *Granular Gases*, Berlin, 2001. Springer. Lecture Notes in Physics 564.

[3] C. S. Campbell. Rapid granular flows. *Ann. Rev. Fluid Mech.*, 22:57, 1990.

[4] I. Goldhirsch and N. Sela. Origin of normal stress differences in rapid granular flows. *Phys. Rev. E*, 54(4):4458, 1996.

[5] N. Sela and I. Goldhirsch. Hydrodynamic equations for rapid flows of smooth inelastic spheres to Burnett order. *J. Fluid Mech.*, 361:41–74, 1998.

[6] J. D. Goddard. Dissipative materials as models of thixotropy and plasticity. *J. Non-Newt. Fluid Mech.*, 14:141, 1984.

[7] R. B. Bird, R. C. Armstrong, and O. Hassager. *Dynamics of Polymeric Liquids*. John Wiley Sons, London, 1977.

[8] J. D. Goddard. Polymer fluid mechanics. *Adv. App. Mech.*, 19:143, 1977.

[9] J. D. Goddard and M. Alam. Shear-flow and material instabilities in particulate suspensions and granular media. *Particulate Science and Technology*, 17:69, 1999.

[10] P. Coussot, Q. D. Nguyen, H. T. Huynh, and D. Bonn. Avalanche behavior in yield stress fluids. *Phys. Rev. Lett.*, 88(17):175501, 2002.

[11] M. A. Hopkins and M. Y. Louge. Inelastic microstructure in rapid granular flows of smooth disks. *Phys. Fluids A*, 3(1):47, 1991.

[12] I. Goldhirsch and G. Zanetti. Clustering instability in dissipative gases. *Phys. Rev. Lett.*, 70(11):1619–1622, 1993.

[13] S. Luding and H. J. Herrmann. Cluster growth in freely cooling granular media. *Chaos*, 9(3):673–681, 1999.

[14] S. B. Savage. Instability of unbounded uniform granular shear flow. *J. Fluid Mech.*, 241:109, 1992.

[15] M. Alam and P. R. Nott. Stability of plane couette flow of a granular material. *J. Fluid Mech.*, 377:99–136, 1998.

[16] J. T. Jenkins and R. W. Richman. Plane simple shear of smooth inelastic circular disks: the anisotropy of the second momnent in the dilute and dense limit. *J. Fluid Mech.*, 192:313, 1988.

[17] J. D. Goddard and A. K. Didwania. Computations of dilatancy and yield surfaces for assemblies of rigid frictional spheres. *Quart. J. Mech. Appl. Math.*, 39:145, 1997.

[18] M. Reiner. A mathematical theory of dilatancy. *Amer. J. Math.*, 67:350, 1945.

[19] C. S. Campbell and A. Gong. The stress tensor in a two-dimensional granular shear flow. *J. Fluid Mech.*, 164:107, 1986.

[20] O. R. Walton and R. L. Braun. Viscosity, granular-temperature, and stress calculations for shearing assemblies of inelastic, frictional disks. *Journal of Rheology*, 30(5):949–980, 1986.

[21] M. P. Allen and D. J. Tildesley. *Computer Simulations of Liquids*. Clarendon Press, Oxford, 1989.

[22] A. W. Lees and S. F. Edwards. The computer study of transport processes under extreme conditions. *J. Phys. C*, 5(6):1921, 1972.

[23] Meheboob Alam and Stefan Luding. Rheology of bidisperse granular media: Uniform shear flow. preprint, 2002.

[24] S. Luding. Global equation of state of two-dimensional hard sphere systems. *Phys. Rev. E*, 63:042201–1–4, 2001.

[25] S. Luding and O. Strauß. The equation of state of polydisperse granular gases. In T. Pöschel and S. Luding, editors, *Granular Gases*, pages 389–409, Berlin, 2001. Springer. cond-mat/0103015.

[26] M. W. Richman. The source of second moment in dilute granular flows of highly inelastic spheres. *J. Rheol.*, 33(8):1293, 1989.

[27] A. Santos, J. M. Montanero, J. Dufty, and J. J. Brey. Kinetic model for the hard-sphere fluid and solid. *Phys. Rev. E*, 57(2):1644, 1998.

[28] J. F. Brady and M. Vivic. Normal stresses in colloidal dispersions. *J. Rheol.*, 39:545, 1995.

[29] D. R. Foss and J. F. Brady. Structure, diffusion and rheology of brownian suspensions by stokesian dynamics simulation. *J. Fluid Mech.*, 407:167, 2000.

[30] S. Luding. Structures and non-equilibrium dynamics in granular media. *Comptes Rendus Academie des Science*, 3:153–161, 2002.

[31] J. G. Kirkwood, F. P. Buff, and M. S. Green. The statistical mechanical theory of transport processes. *J. Chem. Phys.*, 17(10):988, 1949.

[32] S. B. Savage and D. J. Jeffrey. The stress tensor in a granular flow at high shear rates. *J. Fluid. Mech.*, 110:255, 1981.

[33] C. S. Campbell and C. E. Brennen. Computer simulation of granular shear flows. *J. Fluid. Mech.*, 151:167, 1985.

[34] S. McNamara and W. R. Young. Inelastic collapse in two dimensions. *Phys. Rev. E*, 50(1):R28–R31, 1994.

[35] S. Luding and S. McNamara. How to handle the inelastic collapse of a dissipative hard-sphere gas with the TC model. *Granular Matter*, 1(3):113–128, 1998. cond-mat/9810009.

[36] H. Grad. On the kinetic theory of rarefied gases. *Comm. Pure and Appl. Math.*, 2:331, 1949.

[37] J. T. Jenkins and R. W. Richman. Grad's 13-moment system for a dense gas of inelastic spheres. *Arch. Rat. Mech. Anal.*, 87:355, 1985.

[38] S. Jin and M. Slemrod. Regularization of the Burnett equations for rapid granular flows via relaxation. *Physica D*, 150:207, 2001.

[39] E. Ikenberry and C. Truesdell. On the pressures and flux of energy in a gas according to Maxwell's kinetic theory. *J. Rat. Mech. Anal.*, 5:1, 1956.

[40] I. Müller. On the frame dependence of stress and heat flux. *Arch. Rat. Mech. Anal.*, 45:241, 1972.

[41] S. Hess. Structure of liquids and solids in nonequilibrium. *J. de Physique*, 46(C3):191, 1985.

LIST OF FIGURE CAPTIONS

FIG. 1. *a*) A snapshot of the sheared granular system at steady-state. The arrows indicate the displacement of the image boxes. (*b*) Variations of the granular energy T and the calculated shear rate γ_{cal} with time. For an explanation of the system and particle properties, see the text. The parameters for both subplots are $\nu = 0.5$, $e = 0.7$ and $N = 1024$.

FIG. 2. (a) Variation of the first normal stress difference $\mathcal{N}_1$ with the solid volume fraction. The arrows on the left ordinate indicate corresponding analytical values for a two-dimensional granular gas. (b) Variations of $\mathcal{N}_1$, $\mathcal{N}_1^k$ and $\mathcal{N}_1^c$ with ν at $e = 0.7$. In both subplots, the symbols represent the simulation data and the lines are drawn to guide the eye.

FIG. 3. The phase diagram, delineating regions of positive and negative first normal stress difference, in the (ν, e)-plane. The filled circles and triangles represent zeros of $\mathcal{N}_1^c$ and $\mathcal{N}_1$, respectively.

FIG. 4. Snapshots of the sheared system with $e = 0.7$ in the dense limit for different densities: (*a*) $\nu = 0.6$, (*b*) $\nu = 0.7$; (*c*) $\nu = 0.725$; (*d*) $\nu = 0.75$.

FIG. 5. Radial distribution function $g(r)$ plotted against the normalized distance r/σ from sheared simulations with dissipation $e = 0.7$ (solid lines) and from homogeneous, non-sheared situations with $\gamma = 0$ and $e = 1$ (dotted lines): (*a*) $\nu = 0.6$, (*b*) $\nu = 0.7$; (*c*) $\nu = 0.725$; (*d*) $\nu = 0.75$. The arrows indicate the peak values of $g(r)$ at contact for the homogeneous system.

FIG. 6. Variations of the pressure and viscosity functions with density at $e = 0.7$: $f_p = p/\rho T$ and $f_\mu = \mu/\rho\sigma\sqrt{T}$. The lines are drawn to guide the eye.

FIG. 7. Distribution of collision angles $C(\theta)$ for different coefficient of restitutions at $\nu = 0.6$. The symbols represent simulation data and the lines theoretical predictions.

FIG. 8. Polar plots of the collision angle distribution for different densities at $e = 0.7$: (a) $\nu = 0.6$, (b) $\nu = 0.7$; (c) $\nu = 0.725$; (d) $\nu = 0.75$.

FIG. 9. Variations of the average collision angle θ_{av} with density for different restitution coefficients. The arrows indicate densities where $\mathcal{N}_1 \approx 0$. The lines joining the data points are to guide the eye.

FIG. 10. Evidence of *crystallization* in a sheared dense granular fluid at $\nu = 0.8$ and $e = 0.9$. (a) Particle distribution and (b) streamwise velocity at $t = 390$; (c) evolution of streamwise velocity at early times; (d) collision angle distribution.

FIG. 11. Effect of the coefficient of restitution on *crystallization*: $\nu = 0.8$ and $e = 0.99$. (a) Particle distribution and (b) streamwise velocity at $t = 150$; (c) collision angle distribution.

FIG. 12. A schematic of the possible collision angles θ in uniform shear flow; θ is measured anticlockwise from the positive x-axis. Note that the collisions are more likely to occur in the second ($\pi/2 < \theta < \pi$) and fourth ($3\pi/2 < \theta < 2\pi$) quadrants of the colliding disks.

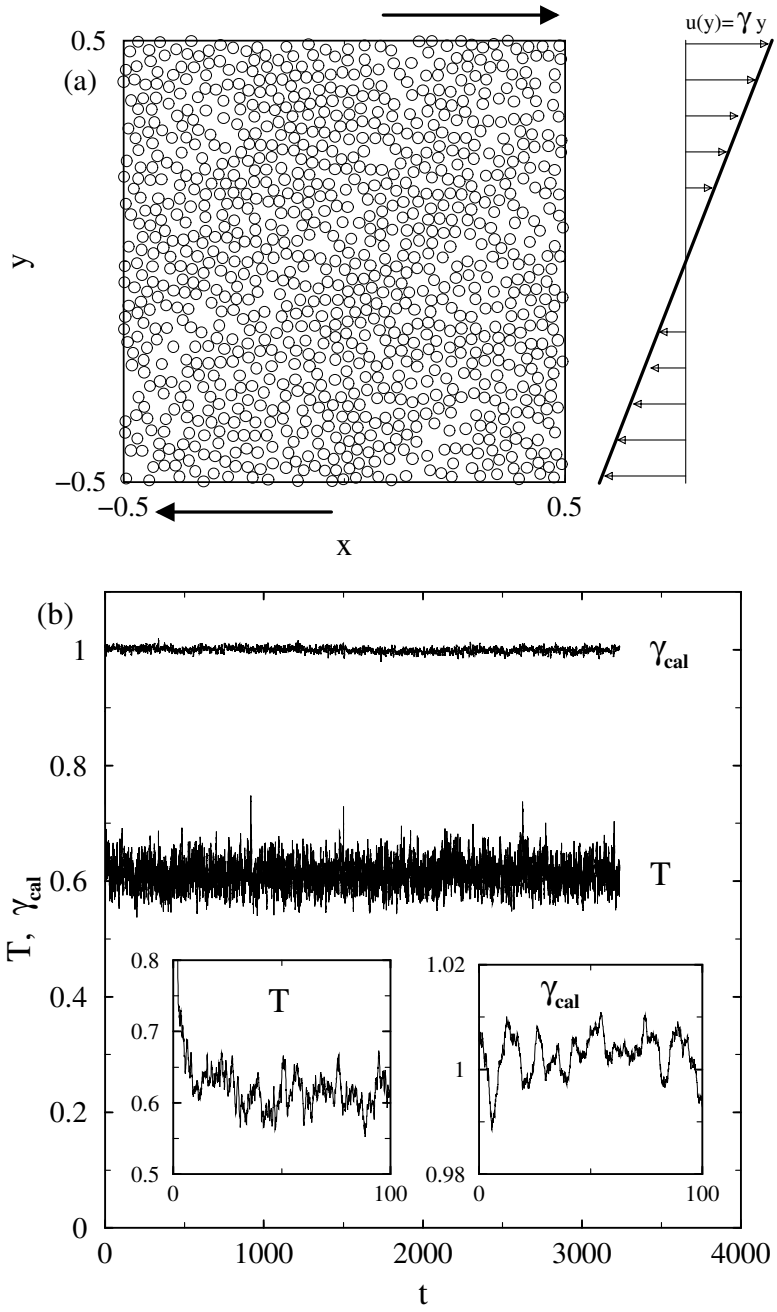

FIG. 1. (a) A snapshot of the sheared granular system at steady-state. The arrows indicate the displacement of the image boxes. (b) Variations of the granular energy T and the calculated shear rate γ_{cal} with time. For an explanation of the system and particle properties, see the text. The parameters for both subplots are $\nu = 0.5$, $e = 0.7$ and $N = 1024$.

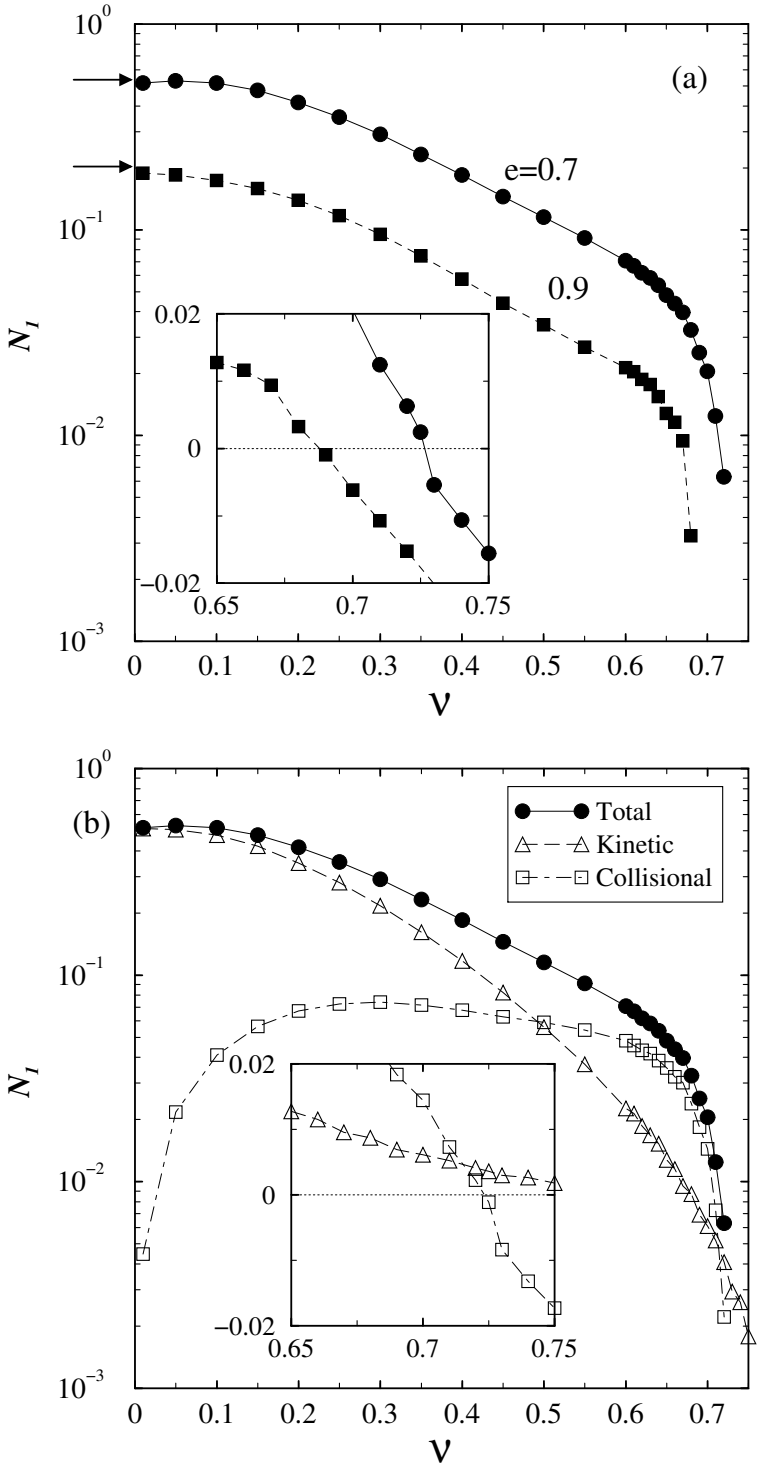

FIG. 2. (a) Variation of the first normal stress difference $\mathcal{N}_1$ with the solid volume fraction. The arrows on the left ordinate indicate corresponding analytical values for a two-dimensional granular gas. (b) Variations of $\mathcal{N}_1$, $\mathcal{N}_1^k$ and $\mathcal{N}_1^c$ with ν at $e = 0.7$. In both subplots, the symbols represent the simulation data and the lines are drawn to guide the eye.

M. Alam (Physics of Fluids)

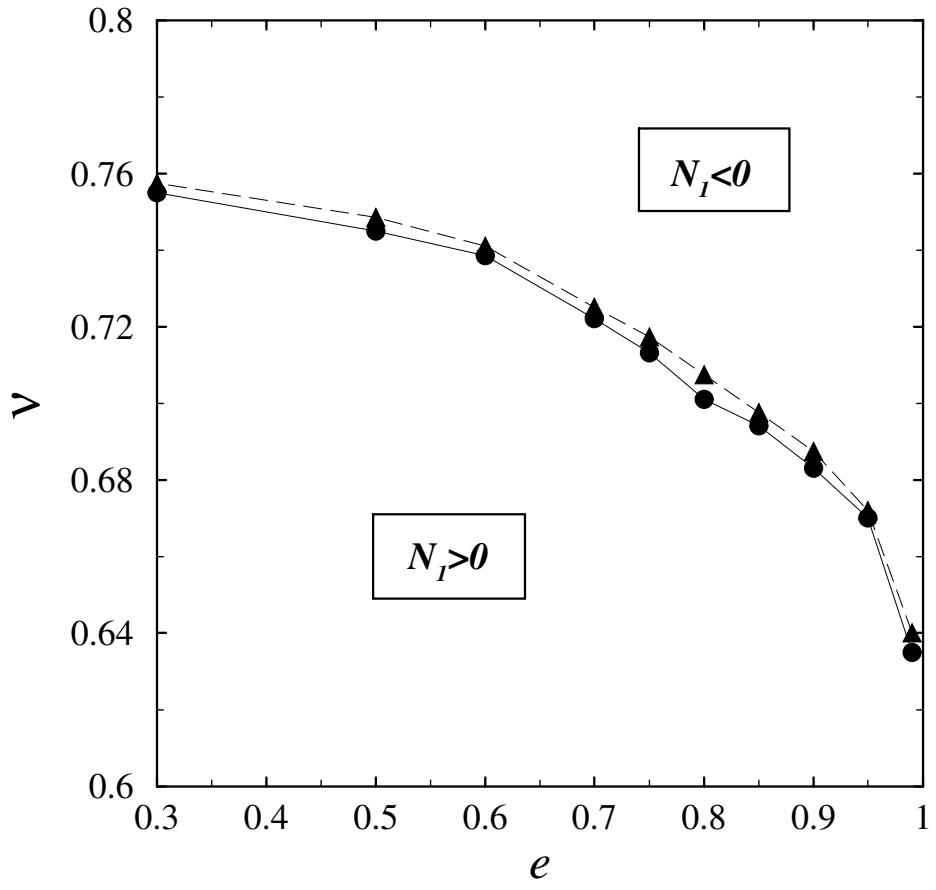

FIG. 3. The phase diagram, delineating regions of positive and negative first normal stress difference, in the (ν, e)-plane. The filled circles and triangles represent zeros of $\mathcal{N}_1^c$ and $\mathcal{N}_1$, respectively.

M. Alam (Physics of Fluids)

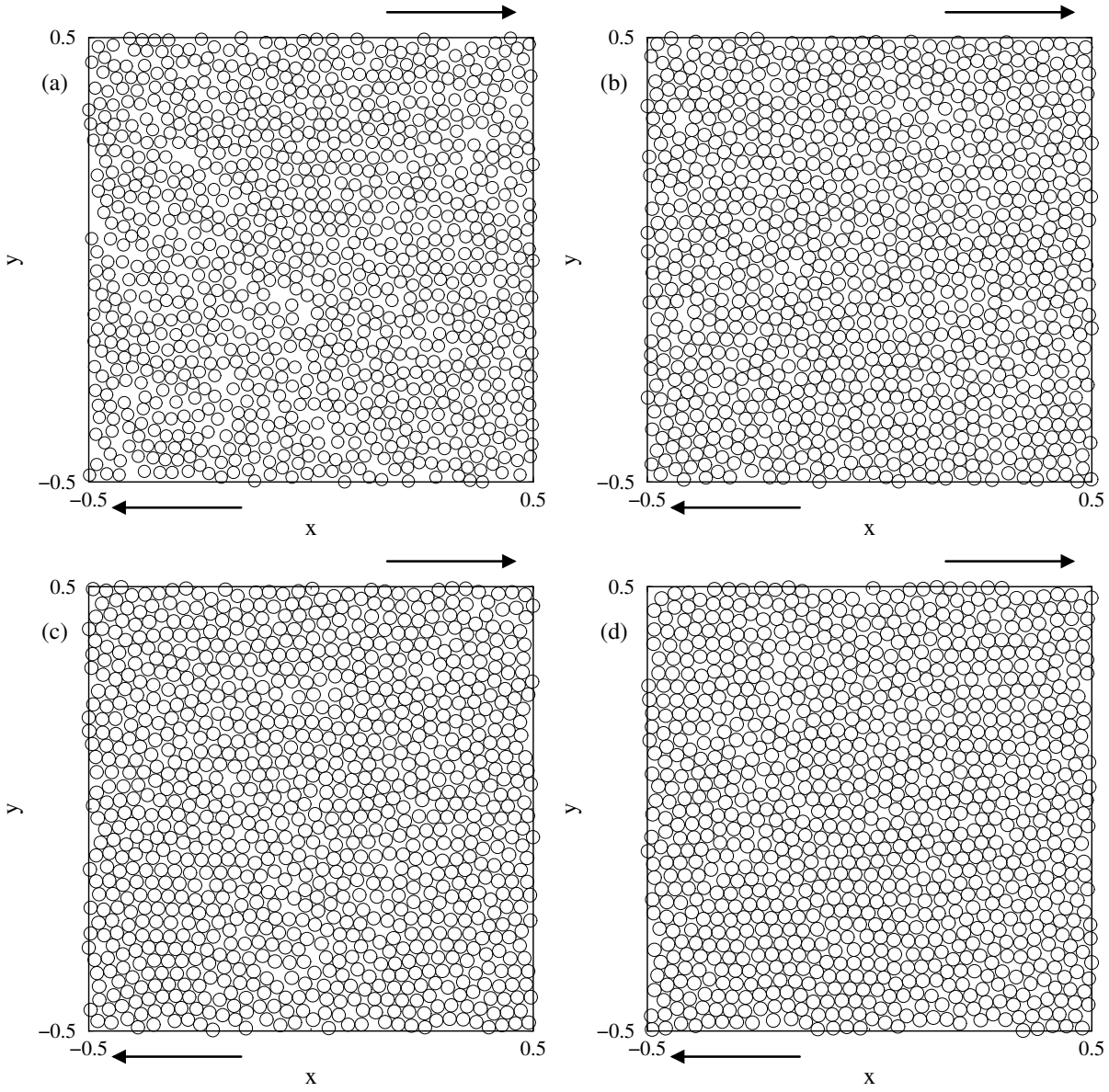

FIG. 4. Snapshots of the sheared system with $e = 0.7$ in the dense limit for different densities: (a) $\nu = 0.6$, (b) $\nu = 0.7$; (c) $\nu = 0.725$; (d) $\nu = 0.75$.

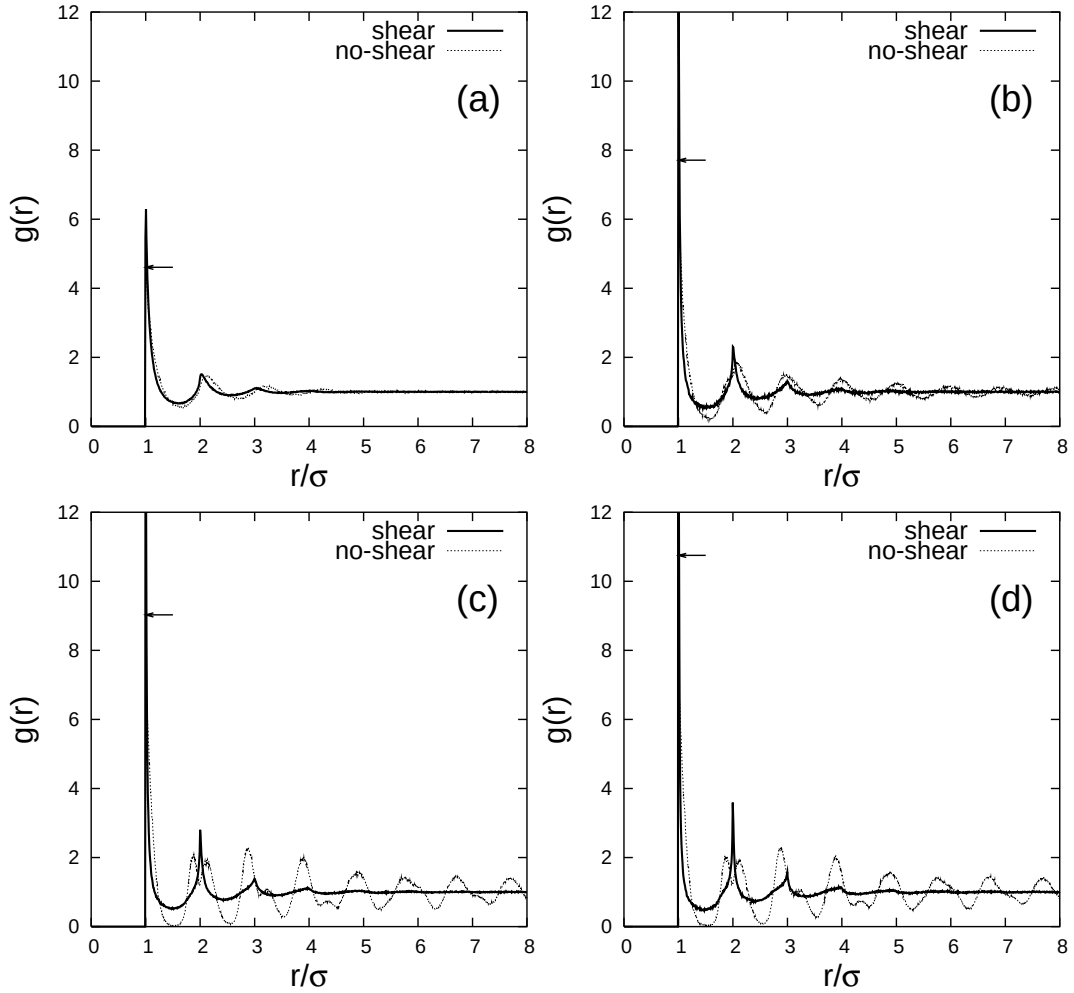

FIG. 5. Radial distribution function $g(r)$ plotted against the normalized distance r/σ from sheared simulations with dissipation $e = 0.7$ (solid lines) and from homogeneous, non-sheared situations with $\gamma = 0$ and $e = 1$ (dotted lines): (a) $\nu = 0.6$, (b) $\nu = 0.7$; (c) $\nu = 0.725$; (d) $\nu = 0.75$. The arrows indicate the peak values of $g(r)$ at contact for the homogeneous system.

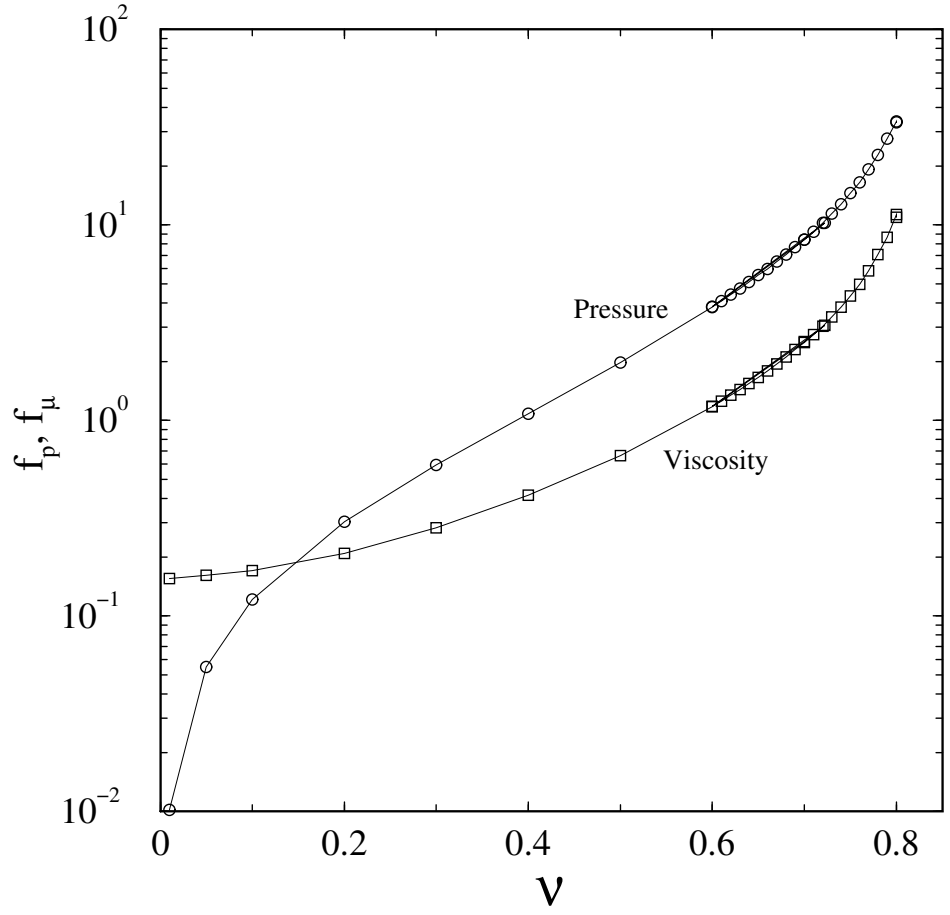

FIG. 6. Variations of the pressure and viscosity functions with density at $e = 0.7$: $f_p = p/\rho T$ and $f_\mu = \mu/\rho\sigma\sqrt{T}$. The lines are drawn to guide the eye.

M. Alam (Physics of Fluids)

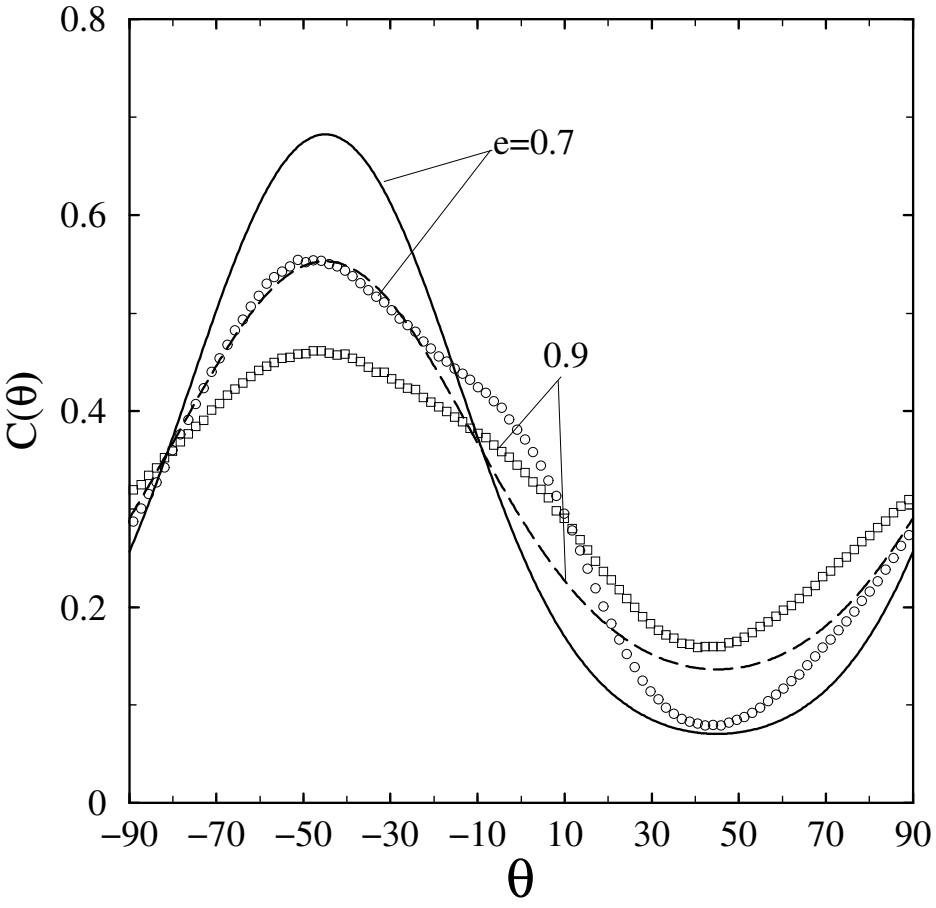

FIG. 7. Distribution of collision angles $C(\theta)$ for different coefficient of restitutions at $\nu = 0.6$. The symbols represent simulation data and the lines theoretical predictions.

M. Alam (Physics of Fluids)

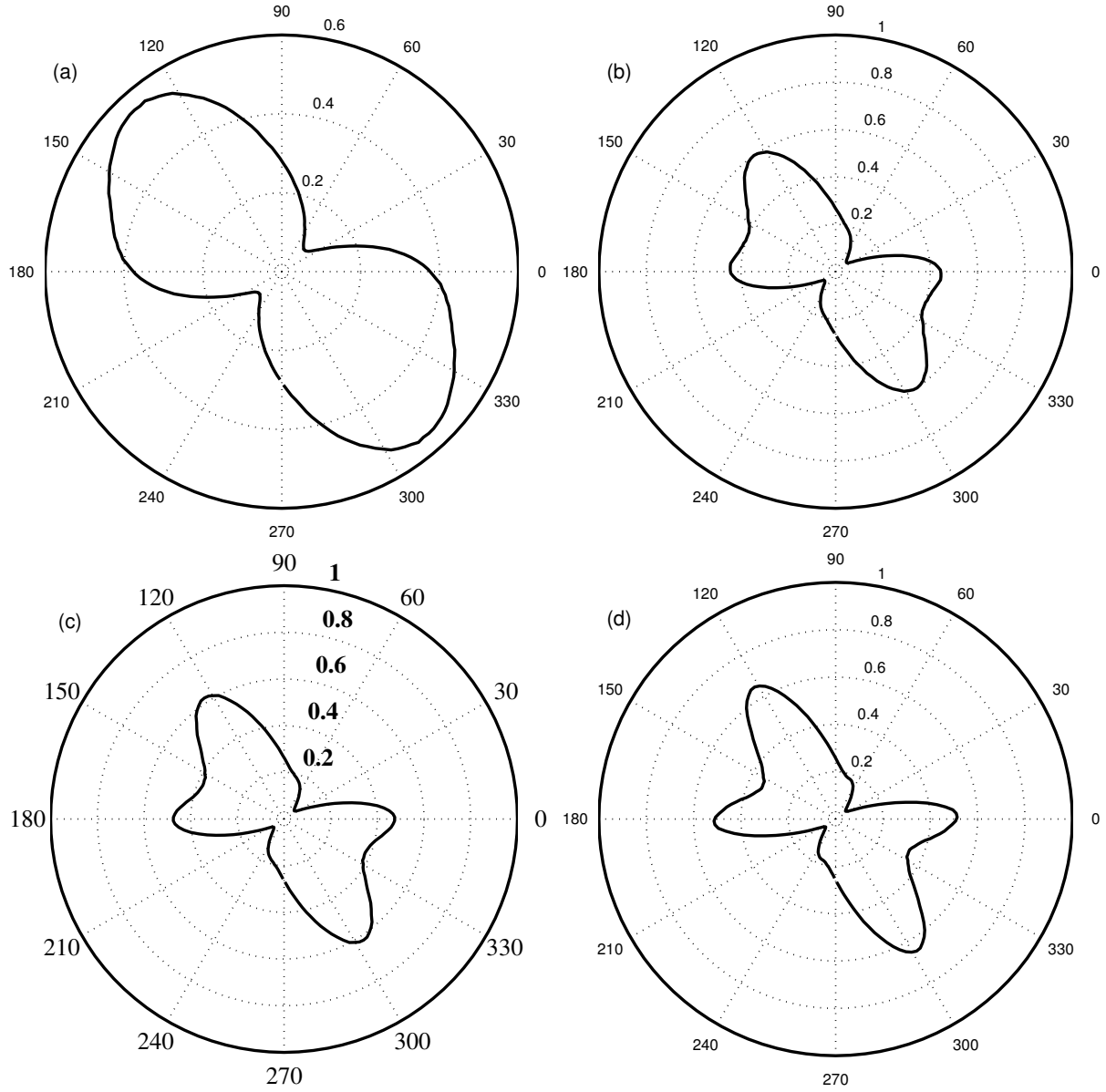

FIG. 8. Polar plots of the collision angle distribution for different densities at $e = 0.7$: (a) $\nu = 0.6$, (b) $\nu = 0.7$; (c) $\nu = 0.725$; (d) $\nu = 0.75$.

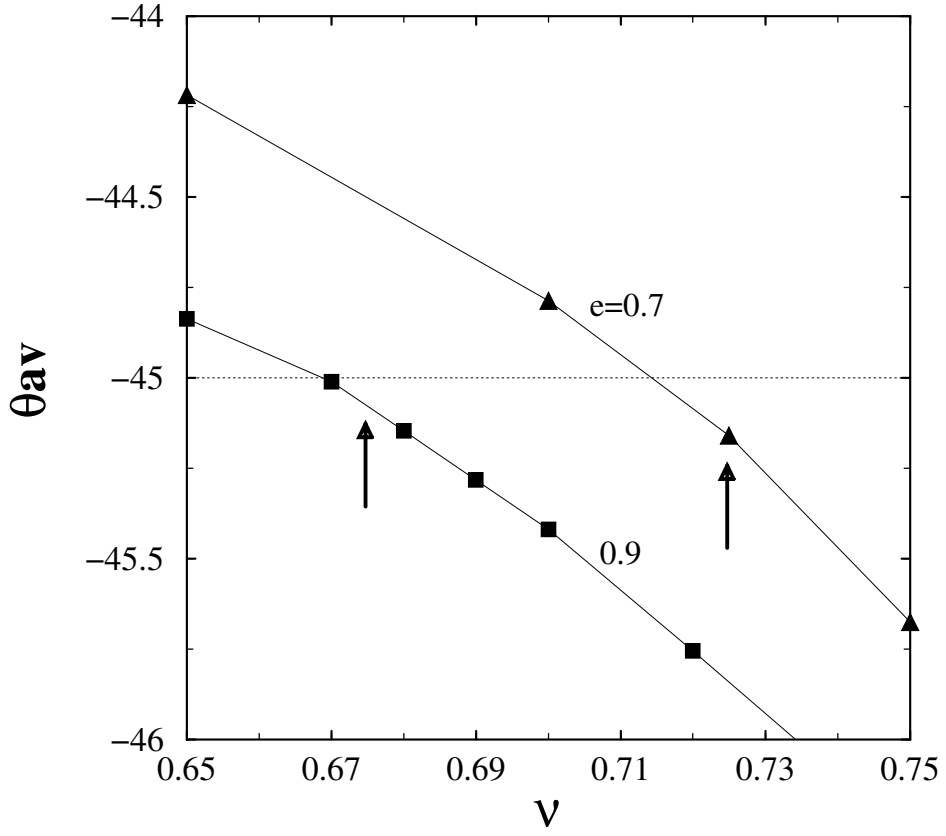

FIG. 9. Variations of the average collision angle θ_{av} with density for different restitution coefficients. The arrows indicate densities where $\mathcal{N}_1 \approx 0$. The lines joining the data points are to guide the eye.

M. Alam (Physics of Fluids)

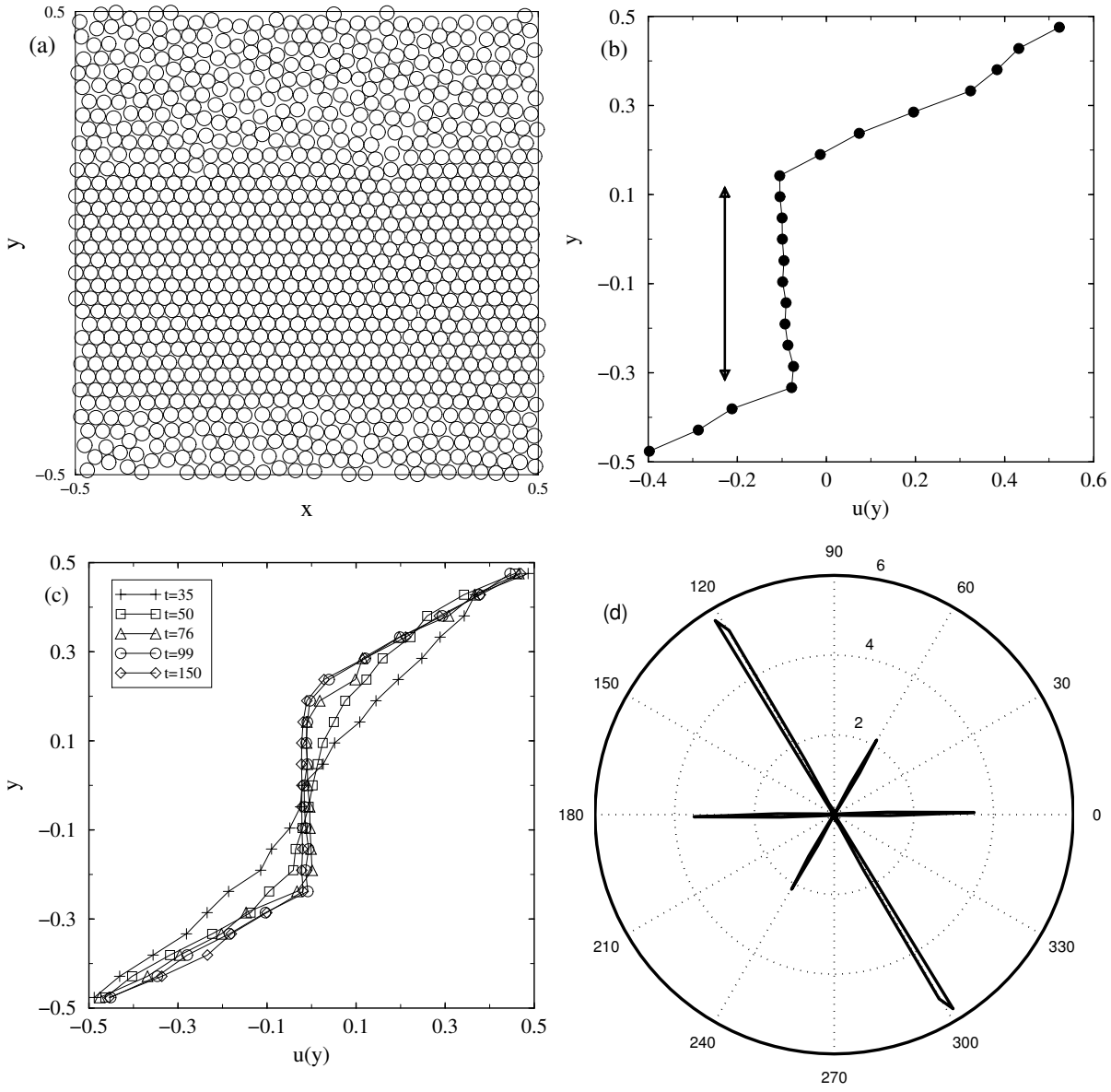

FIG. 10. Evidence of *crystallization* in a sheared dense granular fluid at $\nu = 0.8$ and $e = 0.9$. (a) Particle distribution and (b) streamwise velocity at $t = 390$; (c) evolution of streamwise velocity at early times; (d) collision angle distribution.

M. Alam (Physics of Fluids)

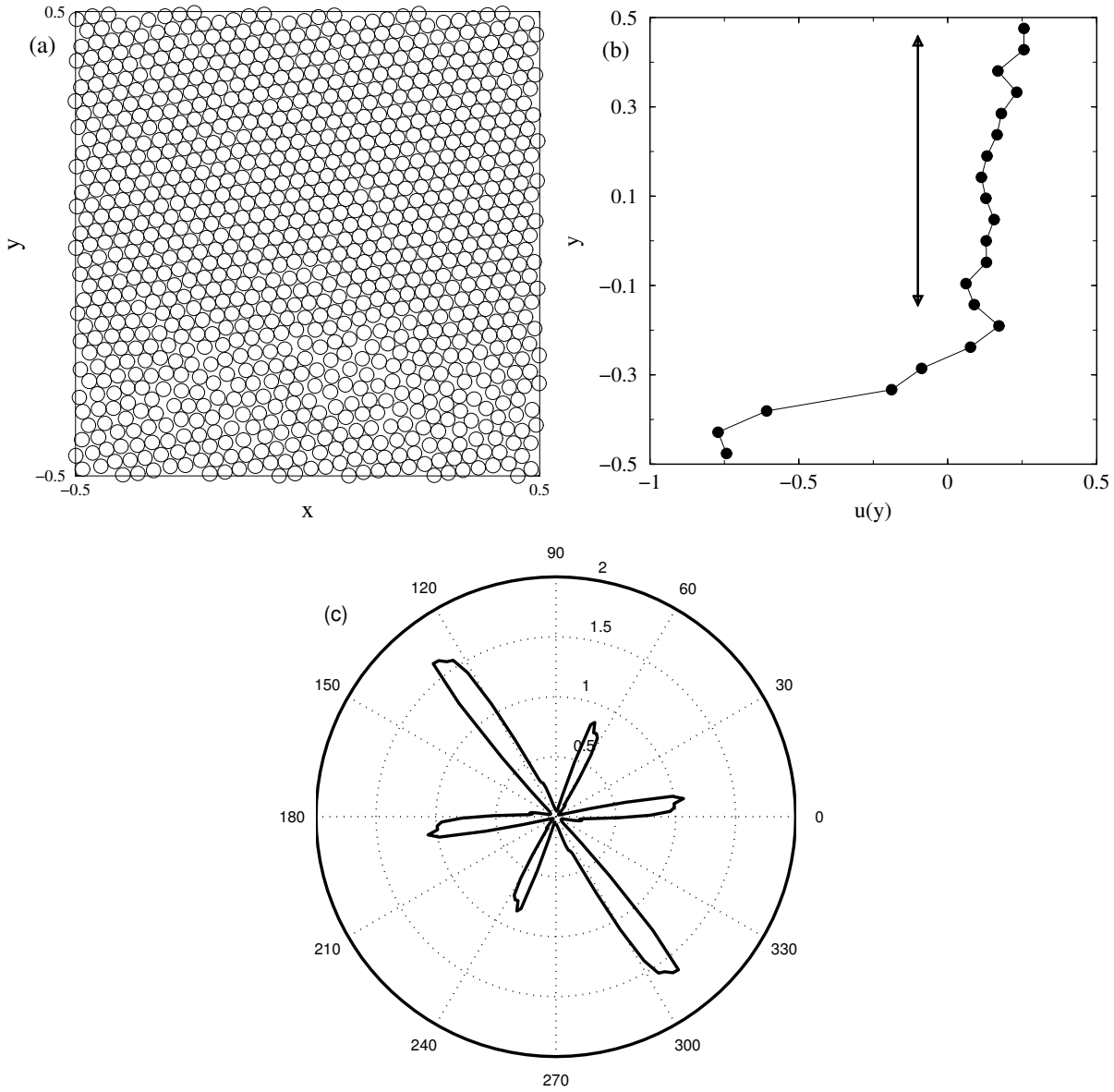

FIG. 11. Effect of the coefficient of restitution on *crystallization*: $\nu = 0.8$ and $e = 0.99$. (a) Particle distribution and (b) streamwise velocity at $t = 150$; (c) collision angle distribution.

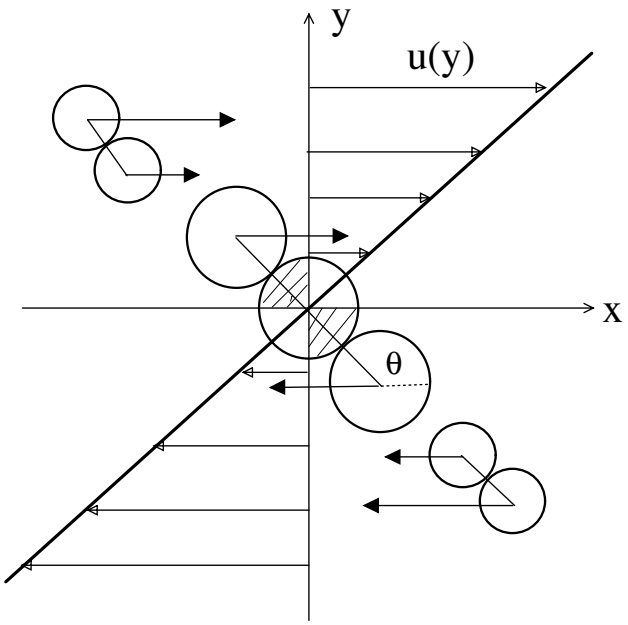

FIG. 12. A schematic of the possible collision angles θ in uniform shear flow; θ is measured anticlockwise from the positive x-axis. Note that the collisions are more likely to occur in the second ($\pi/2 < \theta < \pi$) and fourth ($3\pi/2 < \theta < 2\pi$) quadrants of the colliding disks.

M. Alam (Physics of Fluids)